J. Cent. South Univ. (2020) 27: 388−402
DOI: https://doi.org/10.1007/s11771-020-4304-3

Springer

A novel adsorbent of three-dimensional ordered macro/mesoporous carbon for removal of malachite green dye

WAGN Jie(王杰), HOU Guang-ya(侯广亚), WU Lian-kui(伍廉奎),
CAO Hua-zhen(曹华珍), ZHENG Guo-qu(郑国渠), TANG Yi-ping(唐谊平)

College of Materials Science and Engineering, Zhejiang University of Technology, Hangzhou 310014, China

© Central South University Press and Springer-Verlag GmbH Germany, part of Springer Nature 2020

Abstract: Three-dimensional ordered macro/mesoporous carbon (3DOM/m-C) with high specific surface area was synthesized by colloid crystal template method with chemical activation by KOH and used as the adsorbent for removing malachite green (MG) in aqueous solution. The microstructures of the adsorbents were characterized by FESEM, TEM and BET, and the effects of initial dye concentration, contact time, solution pH, and temperature on adsorption performance were investigated. The results show that the 3DOM/m-C exhibits extremely high adsorption capacity of 3541.1 mg/g within 2 h, which could be attributed to the novel ordered hierarchical structure with mesopores on three-dimensional ordered macroporous carbon walls. And the adsorption behavior conforms to the pseudo-second-order kinetic and Langmuir adsorption isotherm. 3DOM/m-C can be recycled after being desorbed by absolute ethanol, and still maintains a high capacity of 2762.06 mg/g after 5 cycles.

Key words: malachite green; adsorption; three-dimensional ordered macroporous; mesoporous; thermodynamics; kinetics; desorption

Cite this article as: WAGN Jie, HOU Guang-ya, WU Lian-kui, CAO Hua-zhen, ZHENG Guo-qu, TANG Yi-ping. A novel adsorbent of three-dimensional ordered macro/mesoporous carbon for removal of malachite green dye [J]. Journal of Central South University, 2020, 27(2): 388−402. DOI: https://doi.org/10.1007/s11771-020-4304-3.

1 Introduction

Nowadays, the application of dyes in industry becomes more and more extensive. It was reported that 10^5 kinds of commercial dyes have been used in the world, and the annual output of dyes is over 7×10^5 t. However, amount of dye residue in industrial waste water causes severe environment pollution [1−4]. Malachite green (MG) is a common synthetic dye, which belongs to the triphenylmethane dyes, and it is widely used in the textile industry and agriculture and fishery as fungicide. MG is harmful to aquatic organisms and environment, and it affects human health by cancer, aberration, respiratory disease, reproductive system abnormalities and other adverse conditions. However, MG is difficult to be degraded under natural conditions. Therefore, it is becoming a crucial issue to remove MG from industrial waste water [5−8].

For removing dyes, researchers have developed several methods including oxidation, ozonation, electrochemistry, photocatalysis, filtration, flocculation, microbial degradation and etc [9−15]. Adsorption is a facile and effective method for waste water treatment with the advantages of simple operation, low cost, short time and high removal rate [16, 17]. Activated carbon with large pore volume is a good absorbent for

Foundation item: Projects(U1802254, 51871201) supported by the National Natural Science Foundation of China; Project(LY18E040003) supported by the Zhejiang Provincial Natural Science Foundation, China
Received date: 2019-02-15; **Accepted date:** 2019-05-10
Corresponding author: TANG Yi-ping, PhD, Associate Professor; Tel: +86-13806528869; E-mail: tangyiping@zjut.edu.cn; ORCID: 0000-0001-7007-2630

adsorbing dyes. Nevertheless, some dyes with high molecular weight often are clogged in the microporous structure during adsorption process, resulting in the decrease of the adsorption efficiency and hindering the development of activated carbon as adsorbents [18, 19]. Mesoporous carbon with open and mesoporous structure has the potential for solving these problems; compared with activated carbon, it not only has higher transmission efficiency, but also has much higher adsorption capacity. FUENTES-QUEZADA et al [20] synthesized hard carbon powders with hierarchical mesoporous structure that it possessed the maximum adsorption capacity of 431 mg/g for methylene blue. TIAN et al [21] synthesized ordered mesoporous carbon with high specific surface area and pore volume, of which the maximum adsorption capacity for malachite green was 354.5 mg/g. LIU et al [22] prepared mesoporous carbon CMK-5 with ordered structure of which maximum adsorption capacity values for acid red and active black were 731.61 mmol/g and 50.95 mmol/g respectively.

Three-dimensional ordered macroporous (3DOM) structure possesses abundant connected pores and high specific surface area, which facilitates the mass transmission and storage. 3DOM material can be easily prepared by colloid crystal template, and the pore size can range from mesopores to macropores by choosing the size of template. They are widely used in filtration [23], lithium battery materials [24−30], supercapacitors [31, 32], photocatalytic materials [33−35] and etc [36, 37]. In recently, hierarchical structure has attracted the most attention for adsorbents, due to the combination of different adjustable pore sizes. It was believed that hierarchical structure is helpful to improve molecule transport and prevent pore-clogging even provide a synergetic effect [20]. Therefore, it will be an excellent strategy to combine 3DOM with hierarchical structure for adsorption.

In this work, a novel three-dimensional ordered macro/mesopores carbon (3DOM/m-C) adsorbent was presented; the ordered and hierarchical macro/mesopores structure benefits to the transport and adsorption of dye molecules, resulting in high adsorption capacity. The comparison of the two adsorbents of 3DOM/m-C and 3DOM-C for MG removal was studied, and the effects of initial dye concentration, contact time, solution pH, and temperature on adsorption properties were investigated. Moreover, adsorption kinetics and thermodynamic curves were used to reveal the adsorption mechanism. The results obtained in this study are valuable for the new strategies of designing effective porous adsorbent for dyes.

2 Experimental

2.1 Materials

Methyl methacrylate (MMA, 99%), phenol (99%), 2,2-azobisisobutylamidine dihydrochloride (AIBA), anhydrous ethanol, resorcinol (99%), sodium carbonate (99%), tetraethylorthosilicate (TEOS, 99%), sodium hydroxide (99%), potassium hydroxide (99%), hydrochloric acid (37 wt %), and malachite green oxalate ($C_{26}H_{27}N_2O_6$, M_w: 463.5 g/mol) were purchased from Aladdin and without further purification before use. The *L*-lysine (98 wt%) was purchased from Sigma-Aldrich. Deionized water resistance was greater than 18 MΩ·cm.

2.2 Material preparation

A schematic diagram of the preparation process to fabricate 3DOM-C and 3DOM/m-C is shown in Figure 1. Firstly, monodisperse polymethyl methacrylate (PMMA) microspheres were prepared by a typical soap-free emulsion polymerization method [24]. Briefly, 66 g MMA monomer and 266 mL deionized water were uniformly mixed in a three-neck flask. Then, 0.25 g AIBA was added to the above solution at 75 °C. Monodisperse PMMA microspheres with a diameter of about 450 nm were obtained after 2 h with vigorous strring at 75 °C. The self-assembled microsphere templates were fabricated by evaporation at a designated temperature.

Poly-(resorcinol−fomaldehyde) (RF) was used as carbon precursor [32]. Typically, 3.3 g resorcinol and 0.06 g sodium carbonate were dissolved in 4.5 mL formaldehyde solution with strring for 20 min. Porous carbon was synthesized by infiltrating RF precursor into PMMA templates until the templates were transparent, which means that the templates were completely impregnated. Then the template was aged at 85 °C for 24 h. The carbonization of aged composites was performed at

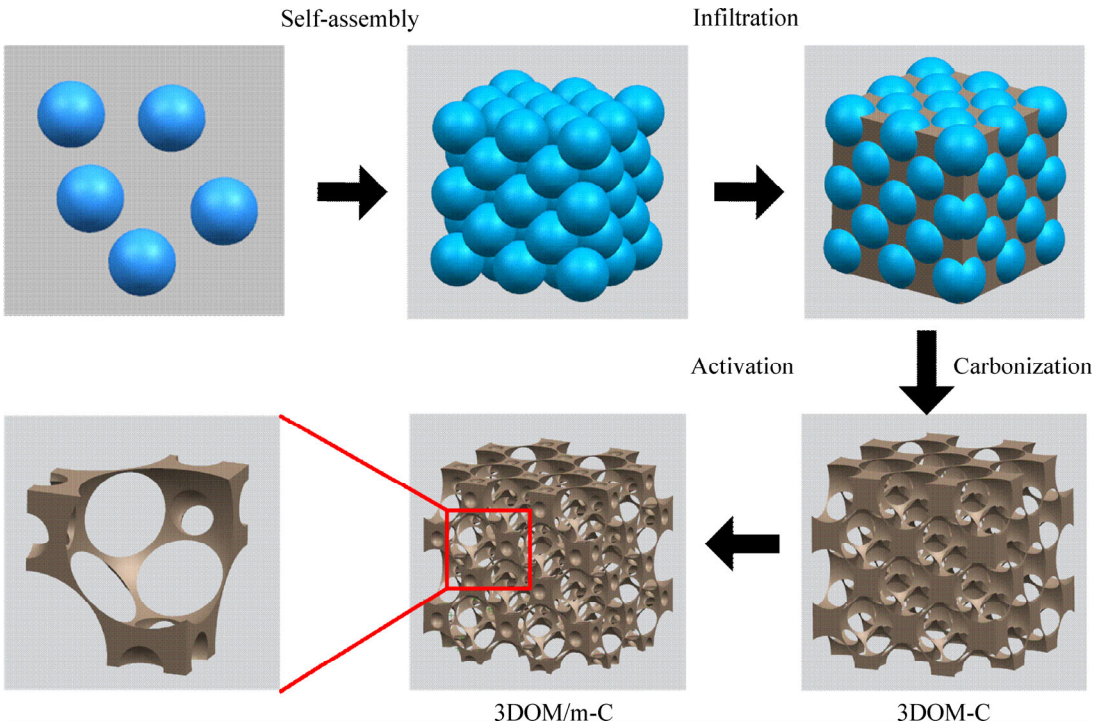

Figure 1 Synthetic illustration of 3DOM-C and 3DOM/m-C

900 °C for 4 h with a heating rate of 5 °C/min and the samples were denoted as 3DOM-C. 3DOM-C was activated by KOH with the weight ratio of KOH to sample about 4:1, at 800 °C for 1.5 h with a heating rate of 5 °C/min under N_2 atmosphere. The obtained samples were wished with 1 mol/L HCl solution and deionized water to remove remaining KOH and it was denoted as 3DOM/m-C.

2.3 Characterization

The morphology of the adsorbents was observed with a field emission electron microscope (Hitachi S-4700, Hitachi, Japan, FESEM) at 10 kV, and transmission electron microscope (Tecnai G2 F30 S-Twin) at an accelerating voltage of 300 kV. N_2 adsorption/desorption isotherms of samples were tested at 77 K using a micromeritics ASAP 2020 analyzer. The samples were outgassed at 473 K for 5 h before measurement. The specific surface area of samples was calculated by the Brunauer−Emmett−Teller (BET) equation; total pore volumes and the pore size distribution were calculated by the Barrett-Joyner-Halenda (BJH) method. Dye concentrations before and after adsorption were characterized by a UV-vis-near-IR scanning spectrophotometer (model UV-1800, Japan) at wavelength of 617 nm. A thermogravimetric analyzer (Netzsch STA449C) was used to determine the weight loss in a N_2 atmosphere at a heating of 5 °C/min.

2.4 Batch adsorption experiments

MG solution with a concentration of 1000 mg/g was accurately prepared in a 500 mL flask, and then different concentrations of MG solution in the adsorption experiment were obtained by diluting it. All adsorption experiments were carried out in a 250 mL Erlenmeyer flask and maintained at 120 r/min in a designated temperature water bath. Typically, 5 mg of the adsorbent was added to 100 mL of 10−400 mg/L MG solution with stirring at a designated temperature for 12 h. Then the adsorbent and solution were separated by centrifugation. The concentration of MG in the solution before and after adsorption was determined under a UV-vis-near-IR scanning spectrophotometer at wavelength of 617 nm. The adsorption amount of MG onto the as-prepared adsorbents was calculated according to the following equation:

$$q_t = \frac{(C_0 - C_t) \times V}{m} \quad (1)$$

where C_0 is the initial concentration of MG (mg/L); C_t is the concentration of MG at contact time t (mg/L); V is the volume of solution (L); m is the

mass of the adsorbents (g). The removal rate of adsorbent in MG solution can be calculated by the following equation:

$$R = \frac{C_0 - C_e}{C_0} \times 100\% \quad (2)$$

where R is the removal rate of MG from solution; C_0 is the initial concentration of MG (mg/L); C_e is the equilibrium concentration of MG solution (mg/L).

In order to investigate the pH_{PZC} of 3DOM/m-C, the experiments were carried out at different pH ranging from 2 to 10 by adjusting with 0.1 mol/L HCl solution and 0.1 mol/L NaOH solution. 0.1 g 3DOM/m-C was added to 50 mL of NaCl solution at different pH and the final pH was detected after magnetic stirring for 24 h.

In order to study the effects of contact time and initial concentration of solution on MG removal, the adsorption capacity at different conditions was recorded. And pH was adjusted with 0.1 mol/L HCl and 0.1 mol/L NaOH solutions. The experiment temperature ranged from 20 to 60 °C.

2.5 Regeneration of adsorbents

The 3DOM/m-C (0.1 g) was mixed with 1 L of 400 mg/L MG solution for 24 h to reach equilibrium, and then the saturated 3DOM/m-C was collected and dried at 60 °C for 24 h. The adsorbed saturated 3DOM/m-C was washed with absolute ethanol. Then, 3DOM/m-C was collected after washing with absolute ethanol for 2 h until the ethanol become colorless. The adsorption−desorption process was repeated five times.

3 Results and discussion

3.1 Adsorbent characterization

Figure 2 shows the thermogravimetric analysis results of the RF@PMMA under nitrogen atmosphere. The RF@PMMA showed a slight weight loss in 100−300 °C which is ascribed to evaporation of low molecular-weight molecules such as free resorcinol, formaldehyde and water [36]. The mass loss occurring in 350−450 °C is attributed to breaking of C—O and C—H bonds in the RF network as well as the degradation of PMMA. The little weight loss occurred in 500−950 °C, indicating that only structural changes took place [37]. Therefore, RF@PMMA can be carbonized completely at 900 °C for 4 h.

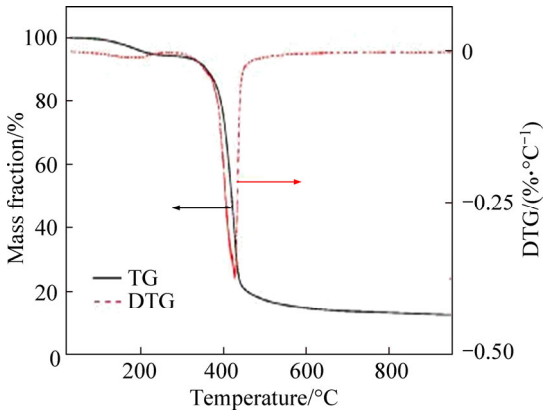

Figure 2 Thermogravimetric analysis of RF@PMMA

The as-prepared PMMA microspheres have uniform size about 500 nm, as shown in Figure 3(a). After self-assembly of evaporation, these microspheres were arranged orderly to form a solid 3D template (Figure 3(b)). Figures 3(c) and (d) exhibit the SEM and TEM images of 3DOM-C, in which the homogeneous macropores and interconnected uniform windows distribute uniformly in the 3D skeleton structure, which are crucial channels for transmission of substances in the sorbents. The skeleton structure of 3DOM-C, which duplicated the ordered structure of colloidal crystal template, reveals obvious shrinkage compared with the original microspheres of templates due to the contraction during calcination. Such a phenomenon has been reported for 3DOM materials [34, 38−40]. In addition, the high-magnification TEM image indicates relatively smooth structure for macroporous carbon wall of 3DOM-C (Figure 3(d)). The skeleton structure of 3DOM/m-C became rough after activation, compared with 3DOM-C, as shown in Figures 3(e) and (f). It is obvious that the 3DOM carbon wall was severely etched to form numerous mesopores, which is beneficial for adsorption of MG dye. Besides, mesopores with the size of about 9 nm can be observed on the macroporous wall as the circles in the insert.

The nitrogen adsorption–desorption isotherms and pore size distribution curves of the porous carbon adsorbents are shown in Figure 4. It can be seen that the two samples exhibit a type II curve with H_3 hysteresis loops in the relative pressure range of 0.8−1.0 as well as a small H_2 type hysteresis loop in the relative pressure range of 0.2−0.8. The N_2 adsorption amounts of 3DOM-C and 3DOM/m-C increased rapidly at low relative

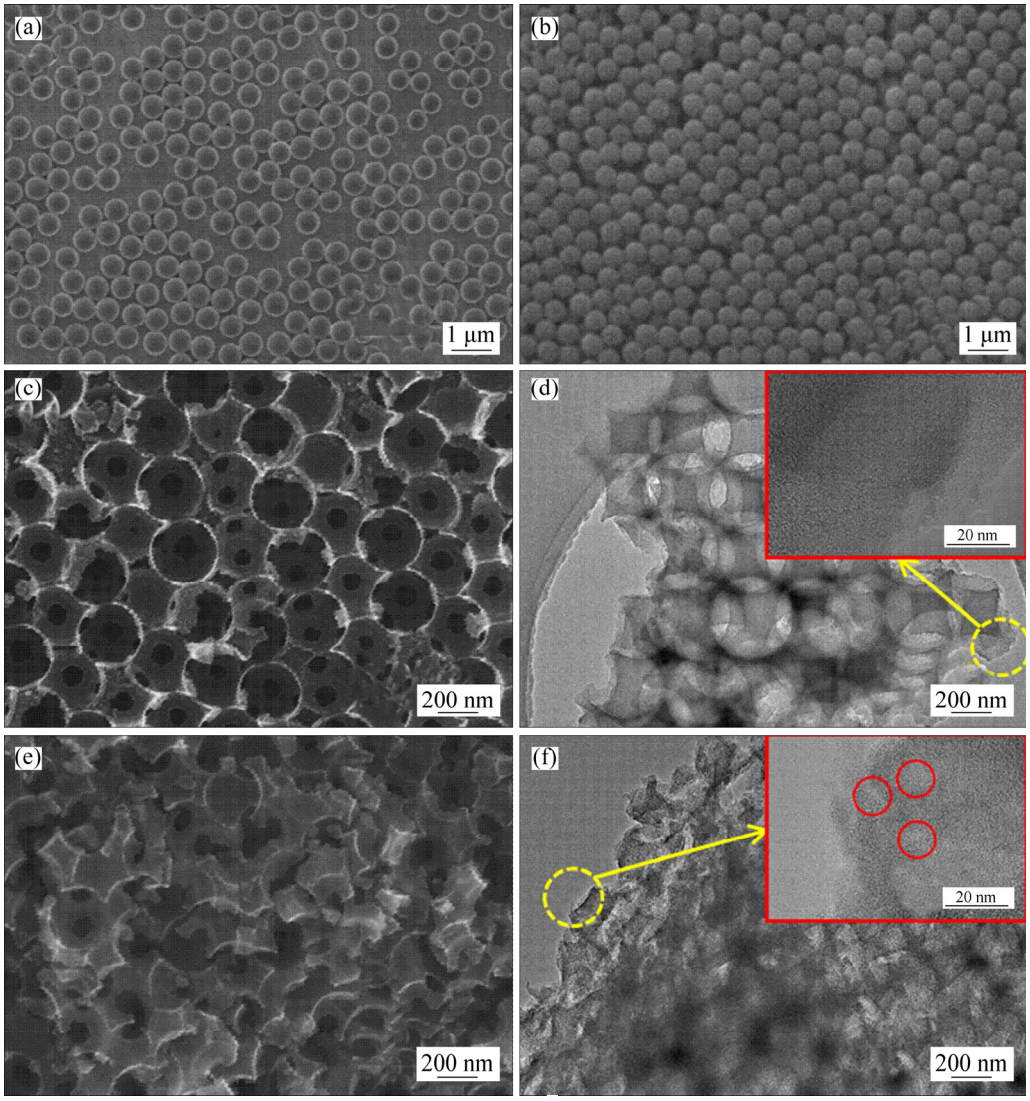

Figure 3 SEM images of prepared PMMA microspheres (a), colloidal crystal template of PMMA microspheres (b), 3DOM-C (c) and 3DOM/m-C (e), TEM images of 3DOM-C (d) and 3DOM/m-C (f)

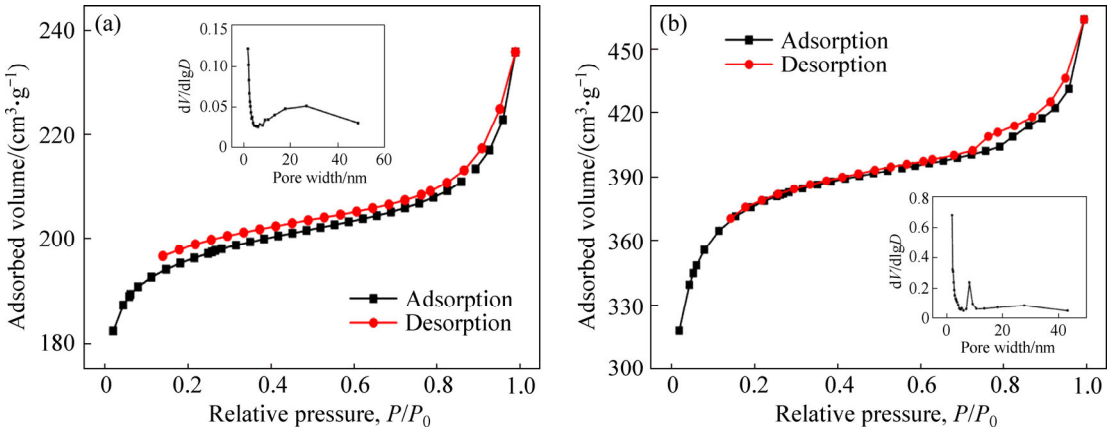

Figure 4 Nitrogen adsorption–desorption isotherms and pore size distribution curves of 3DOM-C (a) and 3DOM/m-C (b)

pressures (<0.1), indicating the presence of micropores produced from the carbonization of RF resol [41]. The N_2 adsorption amounts increased gradually with a small H_2 type hysteresis loop attributed to capillary condensation step in the P/P_0 range of 0.2−0.8, indicating the presence of

mesopores of a variety of sizes in the adsorbent [42]. A H_3 hysteresis loop without any plateau at P/P_0≈1.0 accompanying with marked increase of N_2 adsorption at a P/P_0 above 0.8 was related to the existence of macopores [38]. The pore size distributions also confirmed the existence of abundant mesopores. And the sharp peak is about 9 nm in the inset of Figure 4(b), implying the mesopores generated from activation of KOH, which was consistent with TEM results. Therefore, there are the numerous mesopores on the walls of macropores of 3DOM/m-C, leading to the ultra-high specific surface area of 1414.5 m^2/g and high pore capacity of 0.717 cm^3/g.

3.2 MG adsorption

3.2.1 Effects of contact time and initial concentration

The removal effects of the two adsorbents on MG at different contact times and initial concentrations were investigated. In Figure 5(a), the trends of the two curves are very similar; the amount of adsorption increases rapidly at the early stage and then it becomes slower and finally equilibrium. It could be due to sufficient binding sites on the surface of the adsorbent at the initial stage of adsorption, which increased chances of contact between MG molecules and active sites. In addition, the high MG concentration can provide high driving force. With the proceeding of adsorption process, the active sites on the surface are occupied, and the MG concentration is decreased, resulting in the slow change of the adsorption capacity and eventually reaching equilibrium [43−45]. It can be observed that 3DOM/m-C exhibits the high adsorption capacity (2927.28 mg/g) and removal efficiency (97.58%) at the same initial concentration of MG, far exceeding 3DOM-C. It means that hierarchical structure with mesopores on macroporous walls by activation makes a significant contribution to the adsorption of MG. MG molecules can be transported quickly and efficiently in macropores and then adsorbed in mesopores on the carbon walls, resulting in the high and efficiently adsorption for MG dyes. Therefore, it can be inferred that the adsorption mechanism of MG on 3DOM/m-C is mesopores-filling. In Figure 5(b), the adsorption capacity of 3DOM/m-C increases from 987.0 mg/g to 3541.1 mg/g, and the removal rate of MG decreases from 98.7% to 86.6% (Figure 5(c)). The high initial concentration provides a higher driving force to enhance mass transfer, and the sufficient contact of MG with active site leads to the improvement of adsorption. With the increase of MG concentration, the limited adsorption sites are not enough to accommodate the

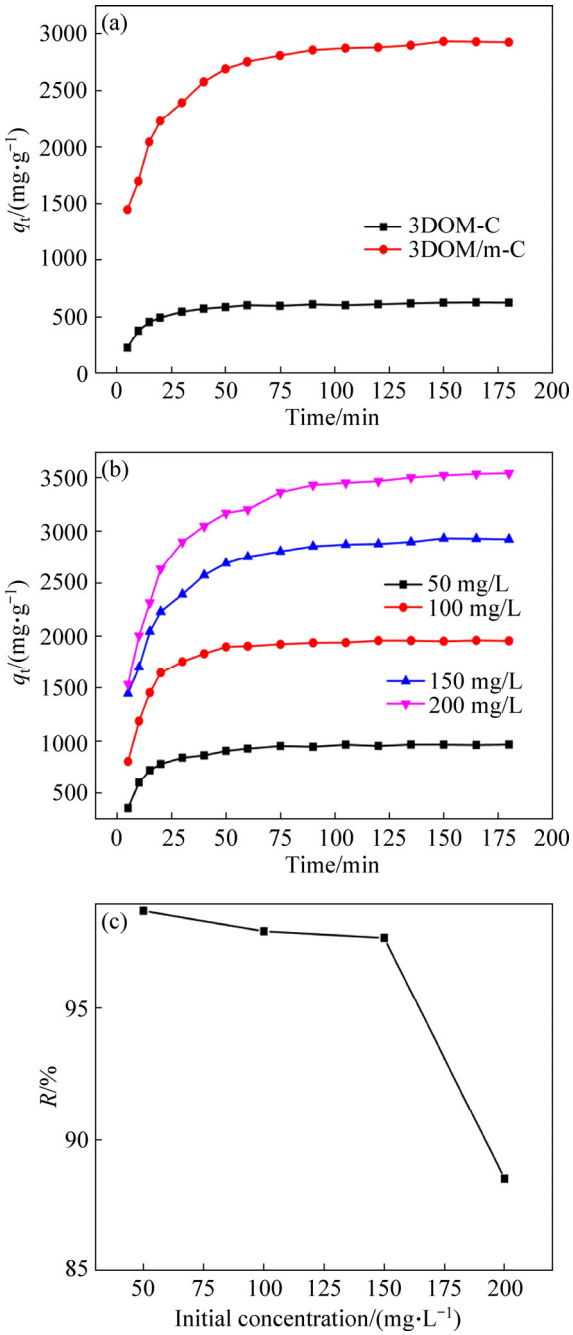

Figure 5 Influence of contact time on adsorption capacity of two adsorbents in MG solution with initial concentration of 150 mg/L (a), adsorption capacity of 3DOM/m-C in MG solution with different initial concentration (50−200 mg/L) (b), removal rates of MG by 3DOM/m-C and 3DOM/m-C with different initial concentration (50−200 mg/L)(c)

rest MG molecules, which is the main reason for the decrease of removal rate. At low-concentration, there are excessive adsorption sites on the surface of adsorbent, which will accelerate the interaction with MG for decreasing the time of equilibrium.

3.2.2 Effects of pH

The point of zero charge (pH_{PZC}) of the adsorbent is an important factor for adsorption. The initial pH of the solution affects MG dye adsorption significantly by affecting the surface charge of the adsorbent and the protonation of MG. The surface charge of adsorbent is positive at $pH<pH_{PZC}$, and it is negative at $pH>pH_{PZC}$. MG is a cationic dye and it is beneficial to adsorption when the surface charge of adsorbent is negative. Figure 6(a) shows pH_{PZC} experimental data for 3DOM/m-C and the pH_{PZC} is 5.9. Figure 6(b) shows the adsorption of MG by 3DOM/m-C at different initial pH. 3DOM/m-C exhibits poor adsorption performance when the initial pH is below 4. There are a large number of protons in solution at low pH. Protons and MG competed for active sites on the adsorbent, resulting in the decrease of adsorption performance.

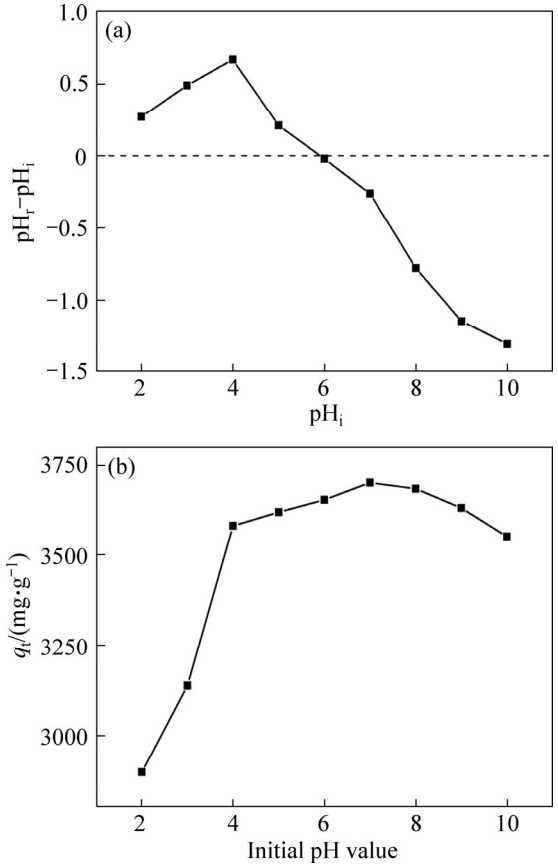

Figure 6 pH_{PZC} experimental data for 3DOM/m-C (a) and adsorption of MG by 3DOM/m-C at different initial pH (b)

At same time, the surface charge of 3DOM/m-C is positive at pH below 5.9, which is harmful to adsorption of MG. When the pH increased from 4 to 7, the surface charge of 3DOM/m-C gradually changed from positive to negative and the protons reduced gradually. This leads to the increase of adsorption capacity. When the pH is above 7, although the negative surface change is beneficial to adsorption, the adsorption capacity slightly decreases due to the combination of MG and —OH, which is similar to the results of ESRA et al [46]. Therefore, the adsorption amount can reach the maximum at pH=7. By studying the effect of pH on adsorption, it can be inferred that the electrostatic attraction is one of the adsorption mechanisms of 3DOM/m-C for MG.

3.2.3 Effect of adsorption temperature

Temperature is also an important factor for MG adsorption. The curves of the adsorption capacity of 3DOM/m-C to MG at different temperatures are shown in Figure 7. It is obvious that the amount of MG adsorption increases with the temperature raising from 20 to 60 °C. At high temperatures, the MG molecules in the solution are more active, increasing the chance of contact with the active site greatly. Moreover, MG molecules are easier to pass through the grain boundary layer and internal pores at high temperature. In addition, the adsorption reaction is an endothermic process, which is more favorable for adsorption at high temperature.

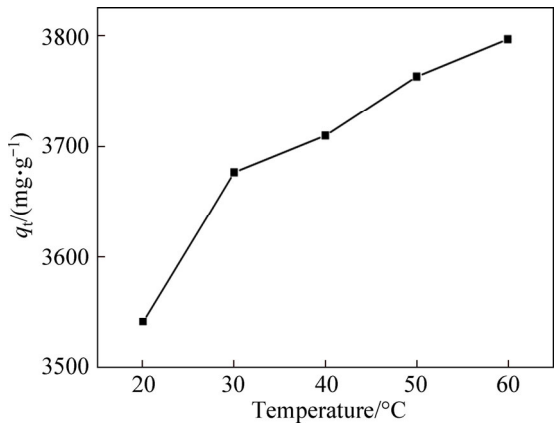

Figure 7 Adsorption of MG by 3DOM/m-C at different temperatures

3.3 Adsorption kinetics

The adsorption process can be described by adsorption kinetics to reveal the possible adsorption mechanism by using pseudo-first-order kinetic

models and pseudo-second-order kinetic models [47, 48]. The pseudo-first-order kinetic model can be expressed by the following equation:

$$\lg(q_e - q_t)=\lg q_e - \frac{k_1}{2.303} \tag{3}$$

where q_e and q_t (mg/L) are the adsorption capacity at equilibrium and the adsorption capacity at time t, respectively; k_1 (min^{-1}) is the pseudo-first-order kinetic adsorption constant. The pseudo-second-order kinetic model is expressed as:

$$\frac{t}{q_t} = \frac{1}{k_2 q_e^2} + \frac{t}{q_e} \tag{4}$$

where k_2 ($g \cdot mg^{-1} \cdot min^{-1}$) is the pseudo-second-order rate constant. The initial adsorption rate V_0 at t=0 can be calculated from Eq. (5).

$$V_0 = k_2 q_e^2 \tag{5}$$

The linear fit results for the kinetic models of the two adsorbents are shown in Figure 8 and Table 1. It can be observed that the calculated value of q_e does not match the experimental data, and the value of R^2 is also lower, which indicates that the adsorption does not conform to the pseudo-first-order kinetics. However, the pseudo-second-order kinetic model is proper; the q_e is close to the experimental value and R^2 is high. The initial adsorption of 3DOM/m-C is higher than that of 3DOM-C, which is main attributed to the higher BET surface and more active sites. MG can be quickly transferred to the surface of the adsorbent due to the presence of macoporous structures, and the number of binding sites ascribed to mesopores on carbon walls determines the speed of adsorption. It indicates the mesopores on macroporous walls after KOH activation promoting the adsorption of MG. The linear fit results of the kinetic model of 3DOM/m-C in different initial concentrations of MG solution are shown in Table 2. Similarly, 3DOM/m-C conforms to the pseudo-second-order kinetic model at various concentrations of MG. From Table 2, it is found that the V_0 increases from 183.15 mg/(g·min) to 444.44 mg/(g·min) when MG concentration increases from 50 mg/L to 200 mg/L. It illustrates that the high concentration of MG provides a higher driving force [49].

In order to explain the adsorption mechanism of MG, the kinetic data were further analyzed by Weber-Morris diffusion model [50]. The model equation is as follows:

$$q_t = k_{di} t^{0.5} + C \tag{6}$$

where k_{di} ($mg \cdot g^{-1} \cdot min^{-1/2}$) is the internal diffusion rate constant and C is a constant related to the boundary thickness. If intra-particle diffusion is the only control step, the curve passes through the origin; if it does not pass through the origin, the adsorption is controlled by the other adsorption stages [51]. In Figure 9, there are three-segment linear regions without pass through the origin for the two adsorbents. It indicates that there are several possible models in the adsorption process. At the initial stage, the MG molecules diffuse onto the outer surface of the adsorbent at high speed. The second stage could be attributed to the slow adsorption of MG molecules that diffuse into the interior of the particles and the extremely low dye concentration residual in the solution. And the third is the equilibrium stage of the MG on the adsorbent [52, 53].

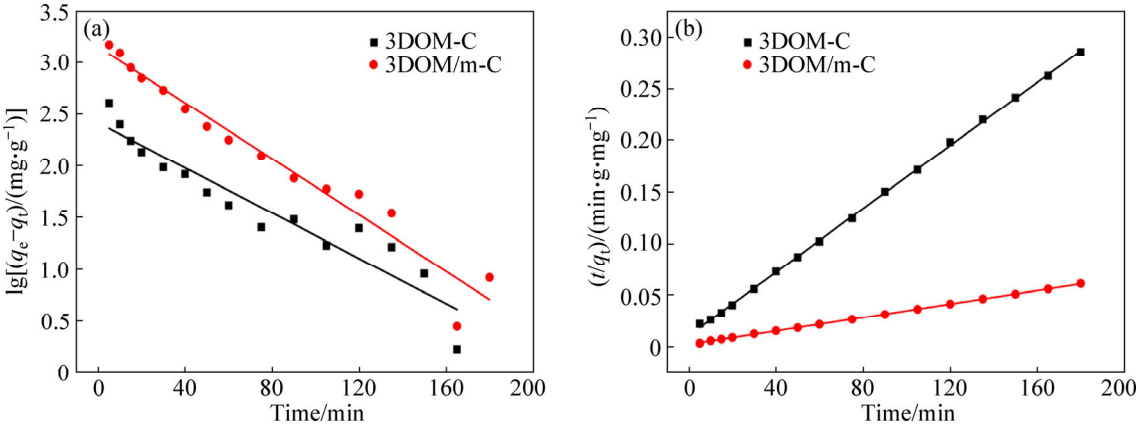

Figure 8 Linear fitting of pseudo-first-order kinetic models of 3DOM-C and 3DOM/m-C (a) and pseudo-second-order kinetic models of 3DOM-C and 3DOM/m-C (b)

Table 1 Pseudo-first-order dynamics model and pseudo-second-order dynamic model fitting parameters of 3DOM-C and 3DOM/m-C in MG solution at initial concentration of 150 mg/L

Sample	q_e/(mg·g^{-1})	Pseudo-first-order kinetic model			Pseudo-second-order kinetic model			
		k_1/min^{-1}	q_{e1}/(mg·g^{-1})	R^2	k_2/(g·mg^{-1}·min^{-1})	q_{e2}/(mg·g^{-1})	R^2	V_0/(mg·g^{-1}·min^{-1})
3DOM-C	628.16	0.02506	258.39	0.8963	2.11×10^{-4}	653.59	0.9996	90.25
3DOM/m-C	2921.69	0.03118	1408.45	0.9520	3.47×10^{-5}	3051.85	0.9998	434.78

Table 2 Pseudo-first-order kinetic model and pseudo-second-order kinetic model fitting parameters of 3DOM/m-C in MG solution at different initial concentrations (50−200 mg/L)

C_0/(mg·L^{-1})	q_e/(mg·g^{-1})	Pseudo-first-order kinetic model			Pseudo-second-order kinetic model			
		k_1/min^{-1}	q_{e1}/(mg·g^{-1})	R^2	k_2/(g·mg^{-1}·min^{-1})	q_{e2}/(mg·g^{-1})	R^2	V_0/(mg·g^{-1}·min^{-1})
50	987.01	0.03844	342.89	0.8334	1.829×10^{-4}	1000.77	0.9993	183.15
100	1958.33	0.03673	682.75	0.8493	9.002×10^{-5}	2032.19	0.9995	371.75
150	2930.10	0.03118	1408.45	0.9520	4.668×10^{-5}	3051.85	0.9998	434.78
200	3541.1	0.03130	1988.29	0.9746	3.223×10^{-5}	3713.36	0.9999	444.44

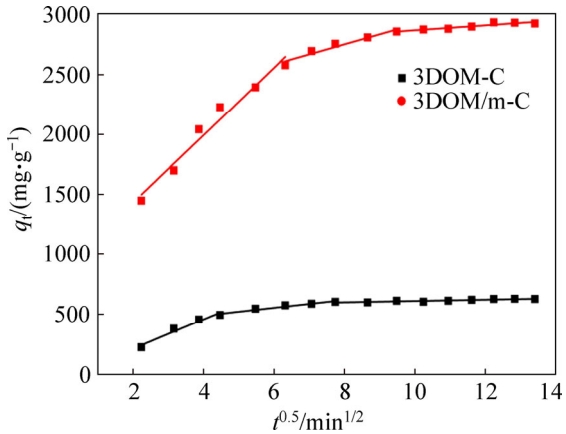

Figure 9 Intra-particle diffusion model of 3DOM-C and 3DOM/m-C

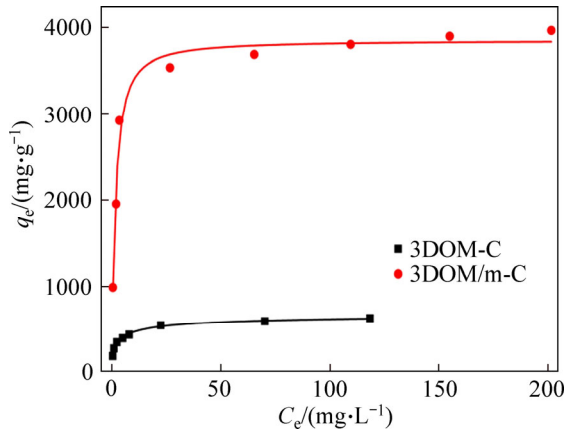

Figure 10 Adsorption isotherms of 3DOM-C and 3DOM/m-C

3.4 Adsorption isotherm

The adsorption isotherm describes the distribution of the adsorbate in the liquid phase and the solid phase at a certain temperature in equilibrium. The adsorption isotherms of the two adsorbents are shown in Figure 10. The Langmuir isotherm model assumes that the adsorption process is a uniform single-layer adsorption [54]. The model equation can be expressed as:

$$\frac{C_e}{q_e} = \frac{1}{q_m k_L} + \frac{C_e}{q_m} \tag{7}$$

where q_e (mg/g) is the equilibrium concentration of the solid phase adsorbate; C_e (mg/L) is the concentration of the adsorbate in the liquid phase at equilibrium; k_L (L/mg) is the equilibrium adsorption constant; q_m (mg/g) is the maximum adsorption amount of the solid phase after complete monolayer adsorption.

Another important adsorption parameter R_L can be calculated by the following formula [55]:

$$R_L = \frac{1}{1 + k_L C_0} \tag{8}$$

where k_L is the Langmuir equilibrium adsorption constant; C_0 is the initial solubility of the adsorbate solution; R_L is the dimensionless parameter. When R_L>1, it indicates that adsorption is not favorable. When 0<R_L<1, it indicates that the adsorption is favorable. When R_L=0, it means that the adsorption is irreversible.

The Freundlich adsorption isotherm describes the multi-layer adsorption of a non-homogeneous phase surface [56], which can be expressed as:

$$\ln q_e = \frac{1}{n} \ln C_e + \ln k_F \tag{9}$$

where k_F (mg/g) and n are adsorption capacity and strength, respectively. The experimental data fitting results of the two models are shown in Figure 11 and Table 3. According to the value of R^2, the Langmuir model is more suitable than the Freundlich model to describe the isotherm adsorption lines of the two adsorbents, and the theoretical maximum capacity of the two adsorbents calculated by the Langmuir model is close to the experimental data. It indicates that the adsorption of MG on the adsorbent is uniform single layer adsorption [54]. In addition, the R_L of the two adsorbents proved to be advantageous for adsorption. The adsorbents prepared in this paper, especially 3DOM/m-C, have an ultra-high MG adsorption capacity, far exceeding the adsorbents reported in other related literatures [44, 57−65]. This is due to the excellent hierarchical macro/mesoporous structure of 3DOM/m-C. The macroporous carbon wall is used as a skeleton to promote the rapid diffusion of MG to the surface of 3DOM/m-C, and the hierarchical structure with abundant mesopores on the carbon wall by KOH activation enables higher specific surface area and larger pore volume, resulting in the ultra-high MG adsorption. The adsorption of MG by 3DOM/m-C and other adsorbents reported is summarized in Table 4. It is clear that the prepared 3DOM/m-C adsorbent is a promising adsorbent.

3.5 Thermodynamic parameters for MG removal by adsorbents

The thermodynamic parameters, including the enthalpy (ΔH), entropy (ΔS), and Gibbs free energy) (ΔG) are studied for evaluating the effects of temperature. The calculating equation is as follows:

$$\ln k_L = \frac{\Delta S}{R} - \frac{\Delta H}{RT} \quad (10)$$

$$\Delta G = -RT\ln k_L \quad (11)$$

$$k_L = \frac{q_e}{C_e} \quad (12)$$

where k_L(L/mg) is the Langmuir constant; ΔS (J·K^{-1}·mol^{-1}) and ΔH (kJ/mol) represent the change of entropy and enthalpy in the adsorption process, respectively; ΔG (kJ/mol) represents the change of Gibbs free energy; q_e is the equilibrium capacity of adsorbent; C_e is the equilibrium concentration of the solution; R is the general gas constant (8.314 J·K^{-1}·mol^{-1}); T is the absolute temperature.

The calculated results are listed in Table 5. In general, the variation of free energy of physical adsorption (0−20 kJ/mol) is smaller than that of chemisorption (80−400 kJ/mol) [16, 66]. It can be seen that ΔG is negative at all temperature (20−60 °C), indicating that the adsorption of the adsorbents is spontaneous and is physical adsorption process. With the increase of temperature, the value of ΔG also becomes more

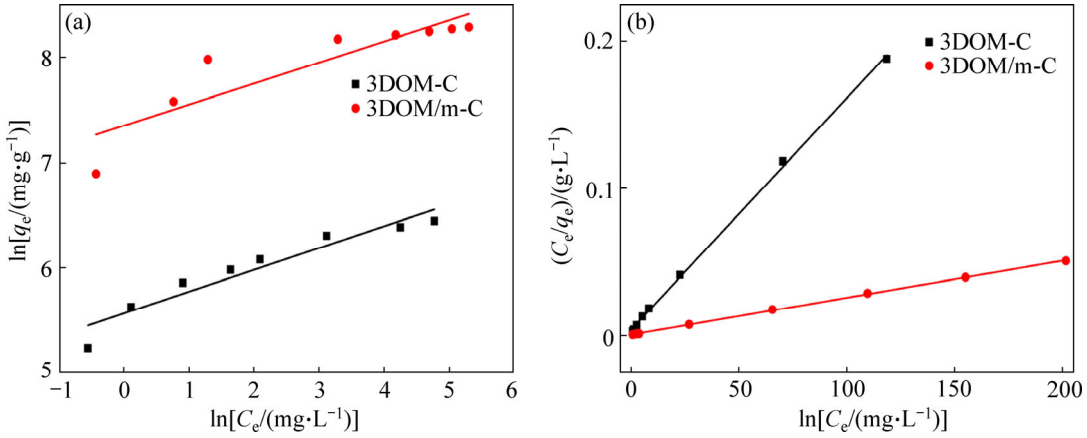

Figure 11 Linear fitting of Freundlich model (a) and linear fit of Langmuir model (b)

Table 3 Langmuir model and Freundlich model fitting parameters for 3DOM-C and 3DOM/m-C

Sample	Langmuir model				Freundlich model		
	q_m/(mg·g^{-1})	k_L/(L·mg^{-1})	R_L	R^2	n	k_F/(L·mg^{-1})	R^2
3DOM-C	636.94	0.377	0.007-0.21	0.9988	4.830	262.43	0.9072
3DOM/m-C	3981.19	0.350	0.007-0.22	0.9994	5.009	1556.20	0.7662

Table 4 Comparison of maximum adsorption capacity of various adsorbents for MG

Adsorbent	q_m/(mg·g^{-1})	Reference
3DOM/m-C	3541.1	This study
Oxidized mesoporous carbon	963.1	[45]
CO_2-activated porous carbon	210.18	[58]
ZnO nanosheets	2587.0	[59]
Zinc carbon foam-like	1250.0	[60]
Zeolitic imidazolate framework nanoparticles	3324.17	[61]
Nickel hydroxide nanoplate loaded on activated carbon	76.92	[62]
Cobalt ferrite-silica nanocomposites	75.5	[63]
Cu-MOFs/Fe_3O_4 composite	113.67	[64]
Magnetic graphene oxide decorated with persimmon tannins composites	560.58	[65]
Magnetic $Sr_{5x}Ba_{3x}(PO_4)_3(OH)/Fe_3O_4$ nanopowder	526	[66]

Table 5 Calculation data of thermodynamic parameters of two adsorbents

Sample	ΔG/(kJ·mol^{-1})					ΔH/(kJ·mol^{-1})	ΔS/(J·K^{-1}·mol^{-1})
	293 K	303 K	313 K	323 K	333 K		
3DOM-C	−3.223	−3.403	−3.623	−3.779	−3.975	2.079	18.095
3DOM/m-C	−12.275	−13.671	−14.427	−15.471	−16.396	28.628	139.600

negative, meaning that the adsorption is easier at high temperature, which is consistent with the results of Figure 7. And compared with 3DOM-C, the value ΔG of 3DOM/m-C is the more negative, which is consistent with the higher adsorption performance of 3DOM/m-C, meaning that the positive effects of hierarchical structure with additional mesopores produce by activation on macroporous walls. The positive ΔH indicates that the adsorption is an endothermic process, and the positive ΔS indicates the increase of the randomness of the substance in the adsorption process [67, 68].

3.6 Regeneration of 3DOM/m-C

The regeneration of 3DOM/m-C was studied. And it is found that the saturated adsorbent can be effectively desorbed in ethanol, which proves that the adsorption of MG on 3DOM/m-C is a physical process. The absorption−desorption processes were conducted 5 times, as shown in Figure 12. 3DOM/m-C exhibits excellent reversible adsorptive performance, and still maintained the maximum adsorption capacity of 2762.06 mg/g (78%) after 5 cycles, which indicates that 3DOM/m-C is a potential adsorbent for MG.

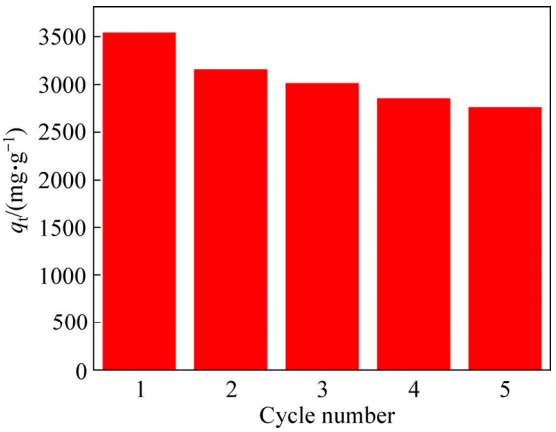

Figure 12 Experimental diagram of 3DOM/m-C cyclic adsorption of MG

4 Conclusions

In summary, a novel adsorbent for MG of 3DOM/m-C with the hierarchical structure with mesopores on ordered macroporous walls was synthesized by colloid crystal template method and chemical activation. The macroporous carbon skeleton provides important transport channels for MG molecule and the mesopores on ordered macroporous carbon walls produced by activation provide sufficient binding sites for MG.

3DOM/m-C exhibits extremely high adsorption capacity of 3541.1 mg/g. The results of BET show that 3DOM/m-C has high specific surface area of 1414.5 m^2/g and large pore volume of 0.717 cm^3/g. And the adsorption behavior conforms to the pseudo-second-order kinetic model and Langmuir adsorption isotherm model. The adsorption of MG is spontaneous; the adsorption process is endothermic; high temperature rise is favorable for adsorption, and the adsorption belongs to physical process. 3DOM/m-C can be regenerated after being desorbed by ethanol, and still maintains a high capacity of 2762.06 mg/g after 5 cycles. The novel adsorbent 3DOM/m-C is a promising adsorbent for MG and other dyes in solution.

References

[1] AHMAD A, MOHD-SETAPAR S H, CHUONG C S, KHATOON A, WANI W A, KUMAR R, RAFATULLAH M. Recent advances in new generation dye removal technologies: Novel search for approaches to reprocess wastewater [J]. RSC Advances, 2015, 5: 30801−30818. DOI: 10.1039/c4ra16959j.

[2] DUTTA R, NAGARJUNA T V, MANDAVGANE S A, EKHE J D. Ultrafast removal of cationic dye using agrowaste-derived mesoporous adsorbent [J]. Industrial & Engineering Chemistry Research, 2014, 53(48): 18558−18567. DOI: 10.1021/ie5030003.

[3] RODRÃ-GUEZ-COUTO S, OSMA J F, TOCA-HERRERA J L. Removal of synthetic dyes by an eco-friendly strategy [J]. Engineering in Life Sciences, 2009, 9(2): 116−123. DOI: 10.1002/elsc.200800088.

[4] GUPTA V, SUHAS. Application of low-cost adsorbents for dye removal — A review [J]. Journal of Environmental Management, 2009, 90(8): 2313−2342. DOI: 10.1016/j.jenvman.2008.11.017.

[5] CHOWDHURY S, MISHRA R, SAHA P, KUSHWAHA P. Adsorption thermodynamics, kinetics and isosteric heat of adsorption of malachite green onto chemically modified rice husk [J]. Desalination, 2011, 265(1−3): 159−168. DOI: 10.1016/j.desal.2010.07.047.

[6] AZAD F N, GHAEDI M, DASHTIAN K, HAJATI S, GOUDARZI A, JAMSHIDI M. Enhanced simultaneous removal of malachite green and safranin O by ZnO nanorod-loaded activated carbon: Modeling, optimization and adsorption isotherm [J]. New Journal of Chemistry, 2015, 39: 7998−8005. DOI: 10.1039/C5NJ01281C.

[7] ASFARAM A, GHAEDI M, GOUDARZI A, SOYLAK M LANGROODI S M. Magnetic nanoparticle based dispersive micro-solid-phase extraction for the determination of malachite green in water samples: optimized experimental design [J]. New Journal of Chemistry, 2015, 39: 9813−9823. DOI: 10.1039/C5NJ01730K.

[8] VYAVAHARE G D, GURAV R G, JADHAV P P, PATIL R R, AWARE C B, JADHAV J P. Response surface methodology optimization for sorption of malachite green dye on sugarcane bagasse biochar and evaluating the residual dye for phyto and cytogenotoxicity [J]. Chemosphere, 2018, 194: 306−315. DOI: 10.1016/j.chemosphere.2017.11.180.

[9] MOREIRA F C, BOAVENTURA R A, BRILLAS E, VILAR V J. Electrochemical advanced oxidation processes: A review on their application to synthetic and real wastewaters [J]. Applied Catalysis B: Environmental, 2017, 202: 217−261. DOI: 10.1016/j.apcatb.2016.08.037.

[10] CLEMATIS D, CERISOLA G, PANIZZA M. Electrochemical oxidation of a synthetic dye using a BDD anode with a solid polymer electrolyte [J]. Electrochemistry Communications, 2017, 75: 21−24. DOI: 10.1016/j.elecom.2016.12.008.

[11] MEERBERGEN K, WILLEMS K A, DEWIL R, IMPE J V, APPELS L, LIEVEMS B. Isolation and screening of bacterial isolates from wastewater treatment plants to decolorize azo dyes [J]. Journal of Bioscience and Bioengineering, 2018, 125(4): 448−456. DOI: 10.1016/j.jbiosc.2017.11.008.

[12] MADHUSUDAN P, ZHANG Jun, CHENG Bei, LIU Gang. Photocatalytic degradation of organic dyes with hierarchical $Bi_2O_2CO_3$ microstructures under visible-light [J]. Crystengcomm, 2012, 15: 231−240. DOI: 10.1039/C2CE26639C.

[13] NIKOOE N, SALJOUGHI E. Preparation and characterization of novel PVDF nanofiltration membranes with hydrophilic property for filtration of dye aqueous solution [J]. Applied Surface Science, 2017, 413(15): 41−49. DOI: 10.1016/j.apsusc.2017.04.029.

[14] HU En-ling, SHANG Song-min, TAO Xiao-ming, JIANG Shou-xiang, CHIU K. Regeneration and reuse of highly polluting textile dyeing effluents through catalytic ozonation with carbon aerogel catalysts [J]. Journal of Cleaner Production, 2016, 137(20): 1055−1065. DOI: 10.1016/j.jclepro.2016.07.194.

[15] LIANG Can-zeng, SUN Shi-peng, LI Fu-yun, ONG Yee-kang, CHUNG Tai-shung. Treatment of highly concentrated wastewater containing multiple synthetic dyes by a combined process of coagulation/flocculation and nanofiltration [J]. Journal of Membrane Science, 2014, 469(1): 306−315. DOI: 10.1016/j.memsci.2014.06.057.

[16] PENG Xiao-ming, HU Xi-jun, FU Da-fang, LAM F L. Adsorption removal of acid black 1 from aqueous solution using ordered mesoporous carbon [J]. Applied Surface Science, 2014, 294(1): 71−80. DOI: 10.1016/j.apsusc.2013.11.157.

[17] GOSCIANSKA J, MARCINIAK M, PIETRZAK R. Ordered mesoporous carbons modified with cerium as effective adsorbents for azo dyes removal [J]. Separation and Purification Technology, 2015, 154(5): 236−245. DOI: 10.1016/j.seppur.2015.09.042.

[18] ZIETZSCHMANN F, WORCH E, ALTMANN J, RUHL A S, SPERLICH A, MEINEL F, JEKEL M. Impact of EfOM size on competition in activated carbon adsorption of organic micro-pollutants from treated wastewater [J]. Water Research, 2014, 65(15): 297−306. DOI: 10.1016/j.watres.2014.07.043.

[19] SÁNCHEZ-SÁNCHEZ A, SUÁREZ-GARCÍA F, MARTÍNEZ-ALONSO A, TASCÓN J. Synthesis, characterization and dye removal capacities of N-doped mesoporous carbons [J]. Journal of Colloid and Interface Science, 2015, 450(15): 91−100. DOI: 10.1016/j.jcis.2015.02.073.

[20] FUENTES-QUEZADA E, LLAVE E, HALAC E, JOBBÁGY M, VIVA F A, BRUNO M M, CORTI H R. Bimodal mesoporous hard carbons from stabilized resorcinol-formaldehyde resin and silica template with enhanced adsorption capacity [J]. Chemical Engineering Journal, 2019, 360(15): 631−644. DOI: 10.1016/j.cej.2018.11.235.

[21] TIAN Yong, LIU Ping, WANG Xiu-fang, LIN Han-sen. Adsorption of malachite green from aqueous solutions onto ordered mesoporous carbons [J]. Chemical Engineering Journal, 2011, 171(3): 1263−1269. DOI: 10.1016/j.cej.2011.05.040.

[22] LIU Feng-ling, GUO Zhao-bing, LING Hu-geng, HUANG Zhong-nian, TANG Deng-yong. Effect of pore structure on the adsorption of aqueous dyes to ordered mesoporous carbons [J]. Microporous and Mesoporous Materials, 2016, 227: 104−111. DOI: 10.1016/j.micromeso.2016.02.051.

[23] LEE P S, HONG D Y, CHA G Y, AN H, MOON S Y, SEONG M, CHANG B J, LEE J S, KIM J H. Mixed matrix membranes incorporated with three-dimensionally ordered mesopore imprinted (3DOm-i) zeolite [J]. Separation and Purification Technology, 2019, 210: 29−37. DOI: 10.1016/j.seppur.2018.07.082.

[24] TANG Yi-ping, SHEN Kang, LV Zi-ye, XU Xin, HOU Guang-ya, CAO Hua-zhen, WU Lian-kui, ZHENG Guo-qu, DENG Yi-da. Three-dimensional ordered macroporous Cu current collector for lithium metal anode: Uniform nucleation by seed crystal [J]. Journal of Power Sources, 2018, 403(1): 82−89. DOI: 10.1016/j.jpowsour.2018.09.083.

[25] TANG Yi-ping, ZHANG Huan-le, LI Ji-quan, HOU Guang-ya, CAO Hua-zhen, WU Lian-kui, ZHENG Guo-qu, WU Qing-liu. Three-dimensional ordered macroporous Cu/Fe_3O_4 composite as binder-free anode for lithium-ion batteries [J]. Journal of Alloys and Compounds, 2017, 719(30): 203−209. DOI: 10.1016/j.jallcom.2017.05.172.

[26] LI Zhen, TAN Yue-yue, HUANG Xiao-xiong, ZHANG Wei, GAO Yi-long, TANG Bo-he-jin. Three-dimensionally ordered macroporous SnO_2 as anode materials for lithium ion batteries [J]. Ceramics International, 2016, 42(16): 18887−18893. DOI: 10.1016/j.ceramint.2016.09.036.

[27] SHEN Kang, WANG Zeng, BI Xuan-xuan, YING Yao, ZHANG Duo, JIN Cheng-bin, HOU Guang-ya, CAO Hua-zhen, WU Lian-kui, ZHENG Guo-qu, TANG Yi-ping, TAO Xin-yong, LU Jun. Magnetic field–suppressed lithium dendrite growth for stable lithium-metal batteries [J]. Advanced Energy Materials, 2019, 9(20): 1900260. DOI: 10.1002/aenm.201900260.

[28] TANG Yi-ping, BI Chao-qi, ZHANG Duo, HOU Guang-ya, CAO Hua-zhen, WU Lian-kui, ZHENG Guo-qu, WU Qing-liu. Three-dimensional ordered macroporous Cu/Sn anode for high rate and long cycle life lithium-ion batteries [J]. Microporous and Mesoporous Materials, 2019, 274: 76−82. DOI: 10.1016/j.micromeso.2018.07.025.

[29] XU Xin, SHEN Kang, WEN Min, WU Qing-liu, HOU Guang-ya, CAO Hua-zhen, WU Lian-kui, ZHENG Guo-qu, TANG Yi-ping. Facile synthesis of three-dimensional Cu/Fe_3O_4 nanowires as binder-free anode for lithium-ion batteries [J]. Applied Surface Science, 2018, 450: 356−363. DOI: 10.1016/j.apsusc.2018.04.089.

[30] TANG Yi-ping, HONG Liang, LI Ji-quan, HOU Guang-ya, CAO Hua-zhen, WU Lian-kui, ZHENG Guo-qu, WU Qing-liu. An internal magnetic field strategy to reuse pulverized active materials for high performance: A magnetic three-dimensional ordered macroporous TiO_2/CoPt/α-Fe_2O_3 nanocomposite anode [J]. Chemical Communications, 2017, 53(38): 5298−5301. DOI: 10.1039/c7cc00940b.

[31] LIU Zhi, MI Jun-hua, YANG Yuan, TAN Xiu-li, LV Cong. Easy synthesis of phosphorus-incorporated three-dimensionally ordered macroporous carbons with hierarchical pores and their use as electrodes for supercapacitors [J]. Electrochimica Acta, 2014, 115: 206−215. DOI: 10.1016/j.electacta.2013.10.161.

[32] VU A, LI Xiao-yue, PHILLIPS J, HAN A, SMYRL W H, BÜHLMANN P, STEIN A. Three-Dimensionally ordered mesoporous (3DOm) carbon materials as electrodes for electrochemical double-layer capacitors with ionic liquid electrolytes [J]. Chemistry of Materials, 2013, 25(21): 4137−4148. DOI: 10.1021/cm400915p.

[33] LI Hao, XIE Qiao, WANG Rui, LI Jun-sheng, XIE Zhi-zhong, TANG Hao-lin. Self-assembled 3DOM macro-/mesoporous TiO_2 photoanode for dye-sensitized solar cells [J]. Applied Surface Science, 2018, 439(1): 1026−1033. DOI: 10.1016/j.apsusc.2017.12.221.

[34] ZHAO Peng, FENG Neng-jie, FANG Fan, LIU Geng, CHEN Li, MENG Jie, CHEN Chong, WANG Lei, WAN Hui, GUAN Guo-feng. Facile synthesis of three-dimensional ordered macroporous $Sr_{1-x}K_xTiO_3$ perovskites with enhanced catalytic activity for soot combustion [J]. Catalysis Science & Technology, 2018, 8(21): 5462−5472. DOI: 10.1039/c8cy01498a.

[35] LIN Bo, YANG Gui-dong, YANG Bo-lun, ZHAO Yu-xin. Construction of novel three dimensionally ordered macroporous carbon nitride for highly efficient photocatalytic activity [J]. Applied Catalysis B: Environmental, 2016, 198(5): 276−285. DOI: 10.1016/j.apcatb.2016.05.069.

[36] SEO J, PARK H, SHIN K, BAECK S H, RHYM Y, SHIM S E. Lignin-derived macroporous carbon foams prepared by using poly(methyl methacrylate) particles as the template [J]. Carbon, 2014, 76: 357−367. DOI: 10.1016/j.carbon.2014.04.087.

[37] LIN Chuan, RITTER J A. Carbonization and activation of sol–gel derived carbon xerogels [J]. Carbon, 2000, 38(6): 849−861. DOI: 10.1016/S0008-6223(99)00189-X.

[38] LI Lu, ZHANG Hong-bo, ZHOU Pin, MENG Xiang-long, LIU Li-zhong, JIA Jin-ping, SUN Tong-hua. Three dimensional ordered macroporous zinc ferrite composited silica sorbents with promotional desulfurization and regeneration activity at mid-high temperature [J]. Applied Surface Science, 2019, 470(15): 177−186. DOI: 10.1016/j.apsusc.2018.11.033.

[39] LI Na, GAN Kai-feng, LU De-li, ZHANG Jin-long, WANG

Ling-zhi. Preparation of three-dimensional macroporous–mesoporous lithium ion sieve with high Li^+ adsorption capacity [J]. Research on Chemical Intermediates, 2018, 44(2): 1105−1117. DOI: 10.1007/s11164-017-3154-6.

[40] LIU Meng-meng, ZHOU Ming-hua, YANG Hui-jia, REN Geng-bo, ZHAO Ying-ying. Titanium dioxide nanoparticles modified three dimensional ordered macroporous carbon for improved energy output in microbial fuel cells [J]. Electrochimica Acta, 2016, 190(1): 463−470. DOI: 10.1016/j.electacta.2015.12.131.

[41] LIU Zhi, TAN Xiu-li, GAO Xin, SONG Li-hong. Synthesis of three-dimensionally ordered macroporous manganese dioxide–carbon nanocomposites for supercapacitors [J]. Journal of Power Sources, 2014, 267(1): 812−820. DOI: 10.1016/j.jpowsour.2014.06.017.

[42] ZHANG Han, DAI Hong-xing, LIU Yu-xi, DENG Ji-guang, ZHANG Lei, JI Ke-meng. Surfactant-mediated PMMA-templating fabrication and characterization of three-dimensionally ordered macroporous Eu_2O_3 and Sm_2O_3 with mesoporous walls [J]. Materials Chemistry and Physics, 2011, 129(1, 2): 586−593. DOI: 10.1016/j.matchemphys.2011.04.073.

[43] KGANDAY W, MARRAKCHI F, ASIF M, GAMEED B. Mesoporous zeolite–activated carbon composite from oil palm ash as an effective adsorbent for methylene blue [J]. Journal of the Taiwan Institute of Chemical Engineers, 2017, 70: 32−41. DOI: 10.1016/j.jtice.2016.10.029.

[44] ZHANG Xia-lan, LIN Qi-lang, LUO Shi-yuan, RUAN Ke-zhao, PENG Kai-ping. Preparation of novel oxidized mesoporous carbon with excellent adsorption performance for removal of malachite green and lead ion [J]. Applied Surface Science, 2018, 442(1): 322−331. DOI: 10.1016/j.apsusc.2018.02.148.

[45] PTASZKOWSKA-KONIARZ M, GOSCIANSKA J, PIETRZAK R. Removal of rhodamine B from water by modified carbon xerogels [J]. Colloids and Surfaces A: Physicochemical and Engineering Aspects, 2018, 543(20): 109−117. DOI: 10.1016/j.colsurfa.2018.01.057.

[46] ALTINTIG E, ONARAN M, SARI A, ALTUNDAG H, TUZEN M. Preparation, characterization and evaluation of bio-based magnetic activated carbon for effective adsorption of malachite green from aqueous solution [J]. Materials Chemistry and Physics, 2018, 220(1): 313−321. DOI: 10.1016/j.matchemphys.2018.05.077.

[47] ZHOU Ying, LIANG Chun-yan, YU Jin-gang, JIANG Xin-yu. Adsorption properties of a novel 3D graphene/MgO composite for heavy metal ions [J]. Journal of Central South University, 2019, 26(4): 813−823. DOI: 10.1007/s11771-019-4051-5.

[48] BHATTI H N, JABEEN A, LQBAL M, NAREEN S, NASEEM Z. Adsorptive behavior of rice bran-based composites for malachite green dye: Isotherm, kinetic and thermodynamic studies [J]. Journal of Molecular Liquids, 2017, 237: 322−333. DOI: 10.1016/j.molliq.2017.04.033.

[49] JIANG Feng, DINH D M, HSIEH Y. Adsorption and desorption of cationic malachite green dye on cellulose nanofibril aerogels [J]. Carbohydrate Polymers, 2017, 173(1): 286−294. DOI: 10.1016/j.carbpol. 2017.05.097.

[50] LEI Chun-sheng, PI Meng, CHENG Bei, JIANG Chuan-jia, QIN Jia-qian. Fabrication of hierarchical porous ZnO/NiO hollow microspheres for adsorptive removal of Congo red [J]. Applied Surface Science, 2018, 435(30): 1002−1010. DOI: 10.1016/j.apsusc.2017.11.201.

[51] KONICKI W, HEŁMINIAK A, ARABCZYK W, MIJOWSKA E. Removal of anionic dyes using magnetic Fe@graphite core-shell nanocomposite as an adsorbent from aqueous solutions [J]. Journal of Colloid and Interface Science, 2017, 497(1): 155−164. DOI: 10.1016/j.jcis.2017.03.008.

[52] KUPFER V L, MANIEZZO R S, LIMA H H C, GUILHERME M R, MOISÉS M P, RINALDI A W. Highly ordered SBA-16 with low nickel amount for enhanced adsorption of methylene blue [J]. Journal of Environmental Chemical Engineering, 2018, 6(4): 3898−3906. DOI: 10.1016/j.jece.2018.06.005.

[53] LEI Chun-sheng, PI Meng, JIANG Chuan-jia, CHENG Bei, YU Jia-guo. Synthesis of hierarchical porous zinc oxide (ZnO) microspheres with highly efficient adsorption of Congo red [J]. Journal of Colloid and Interface Science, 2016, 490: 242−251. DOI: 10.1016/j.jcis.2016.11.049.

[54] RANGABHASHIYAM S, BALASUBRAMANIAN P. Performance of novel biosorbents prepared using native and NaOH treated Peltophorum pterocarpum fruit shells for the removal of malachite green [J]. Bioresource Technology Reports, 2018, 3: 75−81. DOI: 10.1016/j.biteb.2018.06.004.

[55] CHEN Ai-bing, LI Yue-tong, YU Yi-feng, LI Yun-qian, XIA Ke-chan, WANG Yu-ying, LI Shu-hui. Synthesis of mesoporous carbon nanospheres for highly efficient adsorption of bulky dye molecules [J]. Journal of Materials Science, 2016, 51(14): 7016−7028. DOI: 10.1007/s10853-016-9991-7.

[56] PENG Xiao-ming, HUANG Deng-po, ODOOM-WUBAH T, FU Da-fang, HUANG Jia-le, QIN Qing-dong. Adsorption of anionic and cationic dyes on ferromagnetic ordered mesoporous carbon from aqueous solution: Equilibrium, thermodynamic and kinetics [J]. Journal of Colloid and Interface Science, 2014, 430(15): 272−282. DOI: 10.1016/j.jcis.2014.05.035.

[57] YU Miao, HAN Ying-ying, LI Jian, WANG Li-juan. CO_2-activated porous carbon derived from cattail biomass for removal of malachite green dye and application as supercapacitors [J]. Chemical Engineering Journal, 2017, 317(1): 493−502. DOI: 10.1016/j.cej.2017.02.105.

[58] PEI Cui-jin, HAN Guo-ping, ZHAO Yan, ZHAO Hua, BIN Liu, CHENG Li-juan, YANG He-qing, LIU Sheng-zhong. Superior adsorption performance for triphenylmethane dyes on 3D architectures assembled by ZnO nanosheets as thin as ~1.5 nm [J]. Journal of Hazardous Materials, 2016, 318(15): 732−741. DOI: 10.1016/j.jhazmat.2016.07.066.

[59] PRIYANKA M, SARAVANAKUMAR M. Ultrahigh adsorption capacity of starch derived zinc based carbon foam for adsorption of toxic dyes and its preliminary investigation on oil-water separation [J]. Journal of Cleaner Production, 2018, 197: 511−524. DOI: 10.1016/j.jclepro.2018.06.197.

[60] SADAT S A, GHAEDI A M, PANAHIMEHR M, BANESHI M M, BAFAEI A, ANSARIZADEH M. Rapid room-temperature synthesis of cadmium zeolitic imidazolate framework nanoparticles based on 1,1′-carbonyldiimidazole

as ultra-high-efficiency adsorbent for ultrasound-assisted removal of malachite green dye [J]. Applied Surface Science, 2019, 468: 1204−1212. DOI: 10.1016/j.apsusc.2018.10. 274.

[61] NEKOUEI F, KARGARZADEH H, NEKOUEI S, TYAGI I, AGARWAL S, GUPTA V K. Preparation of nickel hydroxide nanoplates modified activated carbon for Malachite Green removal from solutions: Kinetic, thermodynamic, isotherm and antibacterial studies [J]. Process Safety and Environmental Protection, 2016, 102: 85−97. DOI: 10.1016/j.psep.2016.02.011.

[62] AMIRI M, SALAVATI-NIASARI M, AKBARI A, GHOLAMI T. Removal of malachite green (a toxic dye) from water by cobalt ferrite silica magnetic nanocomposite: Herbal and green sol-gel autocombustion synthesis [J]. International Journal of Hydrogen Energy, 2017, 42(39): 24846−24860. DOI: 10.1016/j.ijhydene.2017.08.077.

[63] SHI Zhen-nan, XU Chen, GUAN Han, LI Ling, FAN Lu, WANG Ying-xi, LIU Li, MENG Qing-tao, ZHANG Run. Magnetic metal organic frameworks (MOFs) composite for removal of lead and malachite green in wastewater [J]. Colloids and Surfaces A: Physicochemical and Engineering Aspects, 2018, 539(20): 382−390. DOI: 10.1016/j.colsurfa. 2017.12.043.

[64] GAO Ming-min, WANG Zhong-min, YANG Cheng-xian, NING Jin-liang, ZHOU Zhi-de, LI Gui-yin. Novel magnetic graphene oxide decorated with persimmon tannins for efficient adsorption of malachite green from aqueous solutions [J]. Colloids and Surfaces A: Physicochemical and Engineering Aspects, 2019, 566(5): 48−57. DOI: 10.1016/ j.colsurfa.2019.01.016.

[65] ZHANG Fan, MA Bao-liang, JIANG Xi-ping, JI Yue-fei. Dual function magnetic hydroxyapatite nanopowder for removal of malachite green and Congo red from aqueous solution [J]. Powder Technology, 2016, 302: 207−214. DOI: 10.1016/j.powtec.2016.08.044.

[66] EL-ZAHHAR A A, AWWAD N S. Removal of malachite green dye from aqueous solutions using organically modified hydroxyapatite [J]. Journal of Environmental Chemical Engineering, 2016, 4(1): 633−638.

[67] ZHOU Yan-mei, MIN Ying-hao, QIAO Han, HUANG Qi, WANG En-ze, MA Tong-sen. Improved removal of malachite green from aqueous solution using chemically modified cellulose by anhydride [J]. International Journal of Biological Macromolecules, 2015, 74: 271−277. DOI: 10.1016/j.ijbiomac.2014.12.020.

[68] ABDEL-SALAM A, EWAILS H, BASALEH A. Silver nanoparticles immobilised on the activated carbon as efficient adsorbent for removal of crystal violet dye from aqueous solutions: A kinetic study [J]. Journal of Molecular Liquids, 2017, 248: 833−841. DOI: 10.1016/j.molliq.2017. 10.109.

(Edited by YANG Hua)

中文导读

一种新的三维有序大孔/介孔碳吸附剂对孔雀石绿的去除研究

摘要：采用胶晶模板法和 KOH 化学活化法合成了具有高比表面积的三维有序大孔/介孔碳(3DOM/m-C)，并研究其对溶液中孔雀石绿的去除情况。采用 FESEM、TEM 和 BET 对吸附剂的微观结构进行表征，研究初始染料浓度、接触时间、溶液 pH 值和温度对吸附的影响。结果表明，3DOM/m-C 在 2 h 内吸附容量达到 3541.1 mg/g，这可归因于三维有序大孔碳壁上产生了额外的介孔，形成了有序分级结构。吸附行为符合准二级动力学和 Langmuir 吸附等温模型。吸附完成后，3DOM/m-C 可在无水乙醇脱附并循环使用，在 5 次循环后，吸附容量仍然保持在 2762.06 mg/g。

关键词：孔雀石绿；吸附；三维有序大孔；介孔；热力学；动力学；脱附